Flight path strategies for 3-D scene reconstruction from bistatic SAR

B.D. Rigling and R.L. Moses

Abstract: Proper design of receiver flight paths allows three-dimensional information to be encoded in sensed bistatic SAR phase history data. The authors show how the flight path taken by the receiving platform determines the resolution of nonparametric scene reconstructions and determines the variance of three-dimensional scattering centre location parameter estimates. Based on these relationships, a bistatic SAR data collection strategy can be designed, involving a nonlinear receiver trajectory that allows preservation of three-dimensional scene information.

1 Introduction

Synthetic aperture radar (SAR) is a widely used sensor for all-weather air-to-ground surveillance. Applications for SAR imagery include target detection, recognition and classification. SAR-based automatic target recognition and classification algorithms are hampered by the fact that SAR images are typically two-dimensional reconstructions of the three-dimensional world. For the common case in which a monostatic SAR platform traverses a linear (or nearly linear) aperture, three-dimensional information about the scene of interest is lost in the data collection process [1–3]. To recover 3-D information from linear synthetic apertures, one must have available multiple apertures at different look angles, thereby allowing interferometric [4–6] or stereo [7, 8] processing. Recent works [9–15] have also shown that using a curved aperture in monostatic SAR may allow three-dimensional scene information to be retained without use of multiple SAR platforms, although the curvature required for accurate 3-D localisation of scattering centres may be difficult to achieve in many applications.

An increasing military interest in unmanned aerial vehicle (UAV) technology has sparked renewed interest in bistatic synthetic aperture radar. In bistatic SAR data collection, a transmitting platform and a receiving platform each traverse some flight path with respect to a scene of interest. As in monostatic SAR, when the transmitter and receiver traverse linear flight paths, three-dimensional scene information is lost in the data collection process [16]. This happens when the surface swept out in frequency space by the bistatic line-of-sight (to be defined later) is a plane. All scatterers within the three-dimensional scene project orthogonally onto this data collection plane, in the same manner as defined by the projection-slice theorem for monostatic SAR [3, 16].

As we will show, allowing the transmitter and/or receiver to traverse an out-of-plane nonlinear flight path alters the shape of the data collection surface in frequency space. The degree to which three-dimensional scene information is preserved is determined by the shape, dimensions and orientation of the frequency space manifold. We will quantify the amount of 3-D information retained by considering both nonparametric and parametric methods for scene reconstruction. For a nonparametric reconstruction, the Fourier resolution gives a measure of one's ability to localise a scatterer's position in three dimensions. For parametric reconstructions, the Cramér–Rao lower bound (CRLB), on the variance of the 3-D scattering centre location parameter estimates, provides an information-theoretic measure of the amount of 3-D information stored in a given data set. Based on these two measures for 3-D scene reconstruction quality, we propose a method for designing a receiver's flight path.

2 Bistatic SAR data collection

Consider the bistatic SAR geometry in Fig. 1. The transmitting and receiving platforms each traverse some flight path with respect to a scene of interest, which is centred on the co-ordinate origin. The slant ranges of the transmitter and receiver are denoted as $R_t(\tau)$ and $R_r(\tau)$, and $\phi_t(\tau)$ and $\phi_r(\tau)$ ($\theta_t(\tau)$ and $\theta_r(\tau)$) are their respective azimuth (elevation) angles. The location of the transmitter at a given time τ is

$$\begin{aligned} \boldsymbol{r}_t(\tau) &= [x_t(\tau) \ \ y_t(\tau) \ \ z_t(\tau)]^T \\ &= R_t(\tau)[\cos\phi_t(\tau)\cos\theta_t(\tau) \ \ \sin\phi_t(\tau)\cos\theta_t(\tau) \ \ \sin\theta_t(\tau)]^T \end{aligned} \quad (1)$$

and the location of the receiver is

$$\begin{aligned} \boldsymbol{r}_r(\tau) &= [x_r(\tau) \ \ y_r(\tau) \ \ z_r(\tau)]^T \\ &= R_r(\tau)[\cos\phi_r(\tau)\cos\theta_r(\tau) \ \ \sin\phi_r(\tau)\cos\theta_r(\tau) \ \ \sin\theta_r(\tau)]^T \end{aligned} \quad (2)$$

$\boldsymbol{r}_t(\tau)$ and $\boldsymbol{r}_r(\tau)$ are column vectors. We assume that the transmitter flies a linear path and that the receiver flies an arbitrary curved path. This assumption is motivated by applications in which the transmitter is at (much) longer range to the scene of interest than is the receiver, so a linear approximation of the transmitter flight path is justified. This assumption does not significantly limit the variety of data collection manifolds (defined later) that may be considered, and the results presented below readily extend to the case wherein both the transmitter and receiver traverse nonlinear
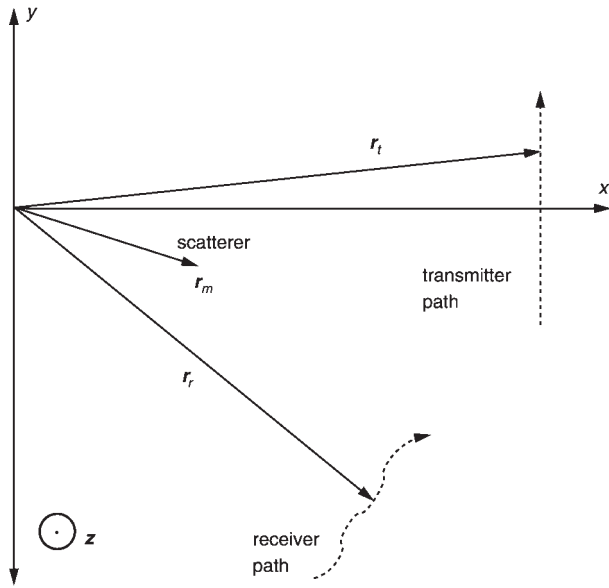
Fig. 1 *Top view a bistatic data collection geometry*
$x-y$ plane is the ground plane

paths. We also assume that motion measurement errors in the system are removed using methods in, e.g. [1, 2, 16], and residual errors result only in image translations without defocus or distortion.

At regular intervals during the data collection period $\tau \in [-T/2, T/2]$, the transmitting platform spotlights the scene of interest with radiated energy. The projected energy is assumed to have uniform power over the frequency range $f \in [f_0, f_0 + B]$, where f_0 is the lowest transmitted frequency, and over the transmitted beam. Reflectors within the scene behave as ideal point scatterers, returning uniform responses at all frequencies $f \in [f_0, f_0 + B]$ and all observation angles. The receiving platform records the reflected responses without introducing any spectral distortions, and gates the recorded data at each look angle such that a scatterer at the origin has zero time delay. We therefore represent the total received signal at slow time τ in the frequency domain as

$$S(f,\tau) = \sum_m A_m \exp\left[-j\frac{2\pi f}{c}\Delta R_m(\tau)\right] + w(f,\tau) \quad (3)$$

where $\Delta R_m(\tau)/c$ is the round-trip time delay to the mth scatterer relative to the round-trip time delay to a scatterer located at the origin and A_m is the complex amplitude of the mth scattering centre. The speed of light is represented by c, and $w(f,\tau)$ is a noise term that includes thermal noise in the receiver and modelling errors (e.g. residual motion measurement errors). In this paper, $w(f,\tau)$ is assumed to be white and Gaussian.

If the imaged scene is small relative to the platform ranges, a far-field assumption accurately approximates the differential range $\Delta R_m(\tau)$ [16]. This approximation may be written as

$$\Delta R_m(\tau) \approx -x_m(\cos\phi_t(\tau)\cos\theta_t(\tau) + \cos\phi_r(\tau)\cos\theta_r(\tau))$$
$$- y_m(\sin\phi_t(\tau)\cos\theta_t(\tau) + \sin\phi_r(\tau)\cos\theta_r(\tau))$$
$$- z_m(\sin\theta_t(\tau) + \sin\theta_r(\tau))$$

$$(4)$$

where the contribution of motion measurement errors [16] has been neglected, under the assumption that their impact on the phase history data may be removed via autofocus in post-processing [1, 2, 16].
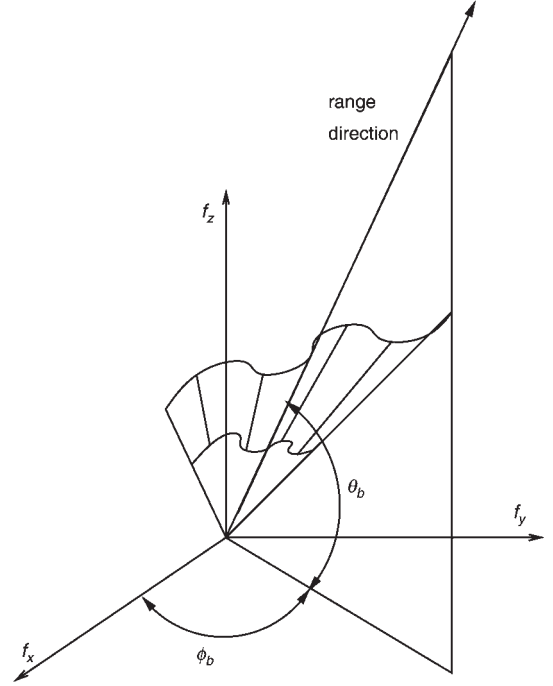

Fig. 2 *Bistatic SAR data collection manifold in 3-D frequency space*

Using (4), our expression for the recorded data (3) may be rewritten as

$$S(f,\tau) \approx \sum_m A_m \exp\left[j\frac{4\pi}{c}\left(x_m f_x(f,\tau) + y_m f_y(f,\tau) + z_m f_z(f,\tau)\right)\right]$$
$$+ w(f,\tau)$$

$$(5)$$

where

$$f_x(f,\tau) = \frac{f}{2}\left(\cos\phi_t(\tau)\cos\theta_t(\tau) + \cos\phi_r(\tau)\cos\theta_r(\tau)\right)$$
$$f_y(f,\tau) = \frac{f}{2}\left(\sin\phi_t(\tau)\cos\theta_t(\tau) + \sin\phi_r(\tau)\cos\theta_r(\tau)\right)$$
$$f_z(f,\tau) = \frac{f}{2}\left(\sin\theta_t(\tau) + \sin\theta_r(\tau)\right)$$

$$(6)$$

The data collection manifold is defined in frequency space as the surface of points $\{(f_x(f,\tau), f_y(f,\tau), f_z(f,\tau))\}$ for $f \in [f_0, f_0 + B]$ and $\tau \in [-T/2, T/2]$. This manifold may also be viewed as the surface swept out by the bistatic line-of-sight, written in vector form as

$$\boldsymbol{u}_{LOS}(\tau) = \frac{1}{2}\begin{bmatrix} \cos\phi_t(\tau)\cos\theta_t(\tau) + \cos\phi_r(\tau)\cos\theta_r(\tau) \\ \sin\phi_t(\tau)\cos\theta_t(\tau) + \sin\phi_r(\tau)\cos\theta_r(\tau) \\ \sin\theta_t(\tau) + \sin\theta_r(\tau) \end{bmatrix}$$

$$(7)$$

as shown in Fig. 2. For future reference, we define the bistatic look angle in azimuth as

$$\phi_b = \tan^{-1}\left(\frac{f_y(f,0)}{f_x(f,0)}\right) \quad (8)$$

and in elevation as

$$\theta_b = \tan^{-1}\left(\frac{f_z(f,0)}{\sqrt{f_x(f,0)^2 + f_y(f,0)^2}}\right) \quad (9)$$

These are the azimuth and elevation angles of the bistatic line-of-sight vector at the midpoint ($\tau = 0$) of the data collection.

3 Nonparametric three-dimensional scene reconstruction

3.1 Scene reconstruction via matched filtering

Given a set of bistatic SAR phase history data $\{S(f_x(f, \tau), f_y(f, \tau), f_z(f, \tau))\}$ for $f \in [f_0, f_0 + B]$ and $\tau \in [-T/2, T/2]$, we now consider nonparametric three-dimensional scene reconstruction. One typically wishes to form an image defined by a uniformly spaced grid of sample points, or voxels, in three-dimensional space. By analysing one voxel at a time, one may assume that a scattering centre is located at each grid location. Then, the value of that voxel is computed as the maximum-likelihood estimate of the complex reflection coefficient $P(x, y, z)$ at that location from the measurements $\{S(f_x(f, \tau), f_y(f, \tau), f_z(f, \tau))\}$. This method is not strictly nonparametric, as it does call for the weak parametric assumption that the scene is composed strictly of point scatterers of unknown amplitude located at the defined voxel centres. Maximum-likelihood estimation of $P(x, y, z)$, for a single scatterer, under the assumption of white Gaussian measurement errors in the phase history data requires minimisation of a least squares cost function written as

$$J = \sum_{i=1}^{N_f} \sum_{k=1}^{N_\tau} \left| S(f_i, \tau_k) - P(x, y, z) \right.$$
$$\left. \times \exp\left[j \frac{4\pi}{c} \left(x f_x(f, \tau) + y f_y(f, \tau) + z f_z(f, \tau) \right) \right] \right|^2$$

(10)

Note that maximum-likelihood estimation of $P(x, y, z)$ for multiple scatterers would require nonlinear least squares minimisation of a similar cost function. Differentiating the cost function J with respect to the real and imaginary parts of $P(x, y, z)$ and setting it equal to zero allows one to solve for the least squares estimate of the voxel value, expressed as

$$P(x, y, z) = \frac{1}{N_f N_\tau} \sum_{i=1}^{N_f} \sum_{k=1}^{N_\tau} S(f_i, \tau_k)$$
$$\times \exp\left[-j \frac{4\pi}{c} \left(x f_x(f, \tau) + y f_y(f, \tau) + z f_z(f, \tau) \right) \right]$$

(11)

The matched filtering (MF) image formation algorithm [16] is given by (11) for each image voxel centred at location (x, y, z).

3.2 Nonparametric scene resolution

The shape and size of the data collection manifold determines the quality of the MF image. The resolution of a two-dimensional scene reconstruction is inversely proportional to the bandwidth of the phase history data in the range and crossrange dimensions [1, 2]. By simple extension to three dimensions, the resolution of the 3-D reconstruction rendered by matched filtering in a particular direction is inversely related to the bandwidth of the frequency space data collection manifold in that same direction.

The relationship between bandwidth and resolution is most clearly seen by considering frequency domain measurements of a scatterer in one dimension, written as

$$S(f_u) = A_0 \exp\left[j \frac{4\pi u_0}{c} f_u \right]$$

(12)

We assume that the data is uniformly sampled over the frequency band $f_u \in [f_0, f_0 + B_u]$, such that these samples may be expressed as $f_u = f_0 + kB_u/N$ for $k = 0 \ldots N - 1$. The 1-D position of the scatterer is u_0. Therefore, the result of the 1-D MF operation is

$$P(u) = \sum_{k=0}^{N-1} \exp\left[j \frac{4\pi u_0}{c} \left(f_0 + \frac{kB_u}{N} \right) \right] \times \exp\left[-j \frac{4\pi u}{c} \left(f_0 + \frac{kB_u}{N} \right) \right]$$
$$= \exp\left[-j \frac{4\pi f_0}{c} (u - u_0) \right] \times \exp\left[-j \frac{2\pi B_u}{c} (u - u_0) \left(1 - \frac{1}{N} \right) \right]$$
$$\times \frac{\sin\left(\frac{2\pi B_u}{c} (u - u_0) \right)}{\sin\left(\frac{2\pi B_u}{cN} (u - u_0) \right)}$$

(13)

Equation (13) yields two observations. First, the quantity $(u - u_0)$ is unambiguously represented in $P(u)$ only over the range $(u - u_0) \in [-cN/(4B_u), cN/(4B_u)]$. This gives the unambiguous range of the reconstruction in the $\hat{u}$ direction. Secondly, the first nulls of $P(u)$ occur at $(u - u_0) = \pm c/(2B_u)$. The Fourier resolution is typically defined to be one-half the mainlobe width [1, 2], implying the MF resolution in the $\hat{u}$ direction is $\delta u = c/(2B_u)$.

Based on the above discussion, the resolution of the 3-D MF reconstruction is most easily analysed by considering the bandwidth of the frequency space manifold in three orthogonal directions. The standard x, y, z co-ordinate system is ill suited for this analysis, as the orientation of the frequency space manifold is rarely oriented along the standard co-ordinate axes. As an alternative, we study three orthogonal directions defined by the geometry of our data collection.

The first and most obvious direction to consider is the range direction defined by the bistatic look angles as $\hat{r} = [\cos \phi_b \cos \theta_b \quad \sin \phi_b \cos \theta_b \quad \sin \theta_b]^T$. The bandwidth of the frequency space manifold in the range direction is equal to the bandwidth of the collected phase histories times the cosine of half the bistatic angle between the transmitter and receiver, defined by

$$\cos \beta = \frac{r_t(0)^T r_r(0)}{\|r_t(0)\| \|r_r(0)\|}$$

(14)

Therefore, the range resolution may be written as

$$\delta r = \frac{c}{2B \cos \beta/2}$$

(15)

We next define the horizontal crossrange direction to be $\hat{h} = [-\sin \phi_b \quad \cos \phi_b \quad 0]^T$, which is orthogonal to the range direction and parallel to the $f_x - f_y$ plane. Note that $(\hat{r}, \hat{h})$ define the traditional slant plane for 2-D image formation. As shown in Fig. 3b, the bandwidth of the frequency space manifold in the horizontal crossrange direction B_H is lower bounded by

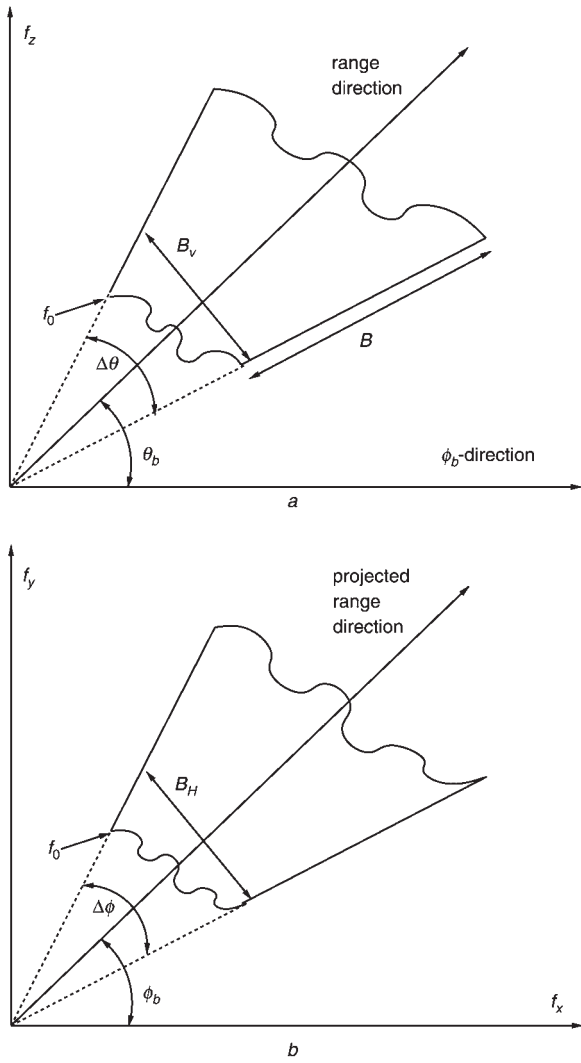$$B_H \geq 2f_0 \sin\left(\frac{\Delta \phi}{2} \right) \cos \theta_b$$

(16)

where

Fig. 3 *Data collection manifold projected in frequency space onto different planes*

a Onto plane defined by f_z-axis and $(\cos\phi_b, \sin\phi_b)$ direction
b Onto $f_x - f_y$ plane

$$\Delta\phi = \max_\tau \tan^{-1}\left(\frac{f_y(f,\tau)}{f_x(f,\tau)}\right)$$
$$- \min_\tau \tan^{-1}\left(\frac{f_y(f,\tau)}{f_x(f,\tau)}\right) \qquad (17)$$

Equation (16) implies that the horizontal crossrange resolution is approximately equal to

$$\delta h = \frac{c}{2B_H}$$
$$= \frac{c}{4f_0 \sin\left(\frac{\Delta\phi}{2}\right)\cos\theta_b} \qquad (18)$$

By default, the vertical crossrange direction is defined to be the direction orthogonal to the previous two directions, and is given by $\hat{v} = [-\cos\phi_b \sin\theta_b \quad -\sin\phi_b \sin\theta_b \quad \cos\theta_b]^T$. As shown in Fig. 3a, the bandwidth of the manifold in this direction is lower bounded below by

$$B_V \geq 2f_0 \sin\left(\frac{\Delta\theta}{2}\right) \qquad (19)$$

where

$$\Delta\theta = \max_\tau \tan^{-1}\left(\frac{f_z(f,\tau)}{\sqrt{f_x(f,\tau)^2 + f_y(f,\tau)^2}}\right)$$
$$- \min_\tau \tan^{-1}\left(\frac{f_z(f,\tau)}{\sqrt{f_x(f,\tau)^2 + f_y(f,\tau)^2}}\right) \qquad (20)$$

This defines the vertical crossrange resolution to be

$$\delta v = \frac{c}{2B_V} = \frac{c}{4f_0 \sin\left(\frac{\Delta\theta}{2}\right)} \qquad (21)$$

Given approximations for the manifold dimensions in the $\hat{r}, \hat{h}$, and $\hat{v}$ directions, one may also approximate the resolutions in the directions of the standard co-ordinate axes through use of the rotation transformation

$$\begin{bmatrix} B_x \\ B_y \\ B_z \end{bmatrix} = \begin{bmatrix} \cos\phi_b \cos\theta_b & \sin\phi_b & \cos\phi_b \sin\theta_b \\ -\sin\phi_b \cos\theta_b & \cos\phi_b & -\sin\phi_b \sin\theta_b \\ -\sin\theta_b & 0 & \cos\theta_b \end{bmatrix} \begin{bmatrix} B \\ B_H \\ B_V \end{bmatrix} \qquad (22)$$

For example, $B_x = B\cos\phi_b \cos\theta_b + B_H \sin\phi_b + B_V \cos\phi_b \sin\theta_b$ implies that the *x*-resolution may be approximated as

$$\delta x \approx \frac{c}{2B_x} = \frac{2}{2[B\cos\phi_b \cos\theta_b + B_H \sin\phi_b + B_V \cos\phi_b \sin\theta_b]} \qquad (23)$$

It is important to note that (15), (18) and (21) approximate the resolution of an ideal three-dimensional reconstruction using matched filtering, by assuming uniform sampling in each direction. The sparse and non-uniform sampling provided by a nonlinear aperture will give an asymmetric, nonseparable ideal point response function. The main lobe widths are well approximated by $2\delta_r, 2\delta_h$ and $2\delta_v$. However, the point response function may have side lobes which are higher than the side lobes corresponding to a filled aperture response. Furthermore, the presence of motion measurement errors during data collection can significantly degrade resolution, especially in the crossrange directions [1, 2, 16]. Nonetheless, (15), (18) and (21) provide (approximate) upper bounds useful for analysis and design.

4 Parametric three-dimensional scene reconstruction

A parametric approach to 3-D scene reconstruction may offer performance that is superior to the above nonparametric method, provided that the associated parameteric assumptions are accurate. For example, we can assume that the scene of interest contains scattering centres that may be represented by members of a library of scattering centre models $\{S_\Theta(f,\tau; \Theta)\}$ parameterised by the elements of the column vector Θ. A simple example of a bistatic SAR scattering model would be a single point reflector in three dimensions

$$S_\Theta(f,\tau; \Theta) = A_1 \exp[j\psi_1]$$
$$\times \exp\left[j\frac{4\pi}{c}\left(x_1 f_x(f,\tau) + y_1 f_y(f,\tau) + z_1 f_z(f,\tau)\right)\right] \qquad (24)$$

where the parameter vector is $\Theta = [A_1, \psi_1, x_1, y_1, z_1]^T$. A richer library class could include canonical scattering

shapes, such as trihedrals, dihedrals, tophats, etc. Similar methods for parametric modelling of monostatic scattering centres [9, 17–19] have shown promise in SAR automatic target recognition applications.

In practice, one assumes that the recorded phase histories may be represented by a superposition of M scattering centres corrupted by additive noise, written as

$$S(f, \tau) = \sum_{m=1}^{M} S_{\boldsymbol{\Theta}}(f, \tau; \boldsymbol{\Theta}) + w(f, \tau) \qquad (25)$$

where $w(f, \tau)$ is white Gaussian noise, independent of the signal terms. Here, $\boldsymbol{\Theta} = [(\boldsymbol{\Theta}^{(1)})^T, \ldots, (\boldsymbol{\Theta}^{(M)})^T]^T$ where, $\boldsymbol{\Theta}^{(m)} = [A_m, \psi_m, x_m, y_m, z_m]^T$ for $m = 1, \ldots, M$. One may then solve for the set of parameters $\hat{\boldsymbol{\Theta}}$, which are assumed to describe the observed scene, through the nonlinear least squares minimisation (with respect to the set of parameters $\hat{\boldsymbol{\Theta}}$)

$$\hat{\boldsymbol{\Theta}} = \arg \min_{\hat{\boldsymbol{\Theta}}} \sum_{i=1}^{N_f} \sum_{k=1}^{N_\tau} \left| S(f_i, \tau_k) - \sum_{m=1}^{M} S_{\boldsymbol{\Theta}}(f_i, \tau_k; \boldsymbol{\Theta}^{(m)}) \right|^2 \qquad (26)$$

If the scene is truly composed of M or fewer scattering centres, all represented in the library of scattering models $\{S_{\boldsymbol{\Theta}}(f, \tau; \boldsymbol{\Theta})\}$, then complete and accurate information about the scene may be extracted. The extracted information provides great versatility with respect to the display of the three-dimensional reconstruction. For example, using the estimated parameters, one may compute the noise-free component of $S(f, \tau)$ at a desired resolution (typically a finer resolution) to be 'imaged' or to be input to a nonparametric estimator, or one may directly display the extracted scattering centres.

4.1 Parametric resolution using the CRLB

The resolution of a parametric model reconstruction is theoretically limited only by the signal-to-noise ratio. Analysis using a Cramér–Rao lower bound [9, 17–19] gives performance limits and serves as a measure to quantify the resolving power of a parametric model reconstruction. Using (24) and (25) and following the methods outlined in [9, 19, 20], we first compute Fisher's information matrix, which for the case of additive white Gaussian noise evaluates to

$$F_{pq} = \frac{2}{\sigma^2} \left(\frac{\partial S_{\boldsymbol{\Theta}}(f, \tau; \boldsymbol{\Theta})}{\partial \boldsymbol{\Theta}_p} \right)^H \left(\frac{\partial S_{\boldsymbol{\Theta}}(f, \tau; \boldsymbol{\Theta})}{\partial \boldsymbol{\Theta}_q} \right) \qquad (27)$$

where $S_{\boldsymbol{\Theta}}(f, \tau; \boldsymbol{\Theta})$ represents the phase history data in vector form and σ^2 is the variance of $w(f, \tau)$. The model parameters are contained in the vector $\boldsymbol{\Theta} = [\theta_1 | \theta_2 | \ldots]$, where each θ_i is a scalar element of $\boldsymbol{\Theta}$ (e.g. in (25) $\theta_1 = A_1$, $\theta_2 = \psi_1$, etc.). The CRLB on the variances of estimates of the parameters in $\boldsymbol{\Theta}$ are then given by the diagonal elements of the inverse of Fisher's information matrix $C_{\boldsymbol{\Theta}} = F^{-1}$, such that $\text{var}(\theta_{ii}) \geq [C_{\boldsymbol{\Theta}}]_{ii}$. A more detailed derivation of the CRLB for the parameters of (24) is given in the Appendix.

Scene reconstruction via parametric modelling comes with some limitations. First and foremost, an accurate reconstruction is dependent on selecting a sufficient number of scattering centres M and on having a library of scattering centres $\{S_{\boldsymbol{\Theta}}(f, \tau; \boldsymbol{\Theta})\}$ that is truly representative of the scene content. Failure in either of these areas may give unpredictable results. Secondly, even if the model order and library of scattering centres is chosen accurately, parametric

models are sensitive to the phase errors introduced by MMEs, even more so than in nonparametric reconstructions. Lastly, solving the nonlinear least squares problem in (26) is computationally intensive, thus limiting the number of scattering centre that may be modelled and the size of the data collection that may be processed.

5 Receiver flight path design

To achieve high-resolution 3-D scene reconstructions, curved receiver paths can be designed to maximise the dimensions of the frequency space manifold described in Section 2. The range resolution is fixed by the transmitter/receiver bandwidth B. However, from (18) and (21), we see that the crossrange resolutions of a matched filtering reconstruction can be manipulated by altering the angular spans of the data collection surface. The horizontal crossrange bandwidth increases with the azimuthal span $\Delta\phi$ of the data collection surface, and the vertical crossrange bandwidth increases with the elevational span $\Delta\theta$ of the data collection surface. Similarly, the resolution of a parametric modelling reconstruction, as defined by the Cramér–Rao lower bounds on location estimates, can be affected through choice of the data collection surface. The following design examples illustrate how varying the receiver flight path may be used to adjust the angular span of the frequency space manifold and to alter the CRLB on scatterer location estimation.

In this simulation, the transmitting platform traverses a straight and level flight path centred on and orthogonal to the positive X-axis, and the receiver's trajectory is similarly symmetric over the positive X-axis, but is shorter and at closer range, with altitude 3 km and ground range 8 km. The transmitter altitude is 10 km, and its ground range is 30 km.

In the first example, we maintain a constant receiver altitude but add curvature to the receiver flight path by varying it in the quadratic form

$$x_r(\tau) = x_r(0) - \alpha y_r(\tau)^2 \qquad (28)$$

where α controls the eccentricity of the receiver's trajectory. Recall that the receiver's position vector is $\boldsymbol{r}_r(\tau) = [x_r(\tau) \quad y_r(\tau) \quad z_r(\tau)]^T$. Figure 4 shows receiver flight paths for values of α of 0–0.0331.

The effect of increased flight path eccentricity on the angular spans is shown in Fig. 5a, and the resultant resolution of a nonparametric 3-D reconstruction are shown in Fig. 5b. Figure 6 shows the square root of the diagonal elements of
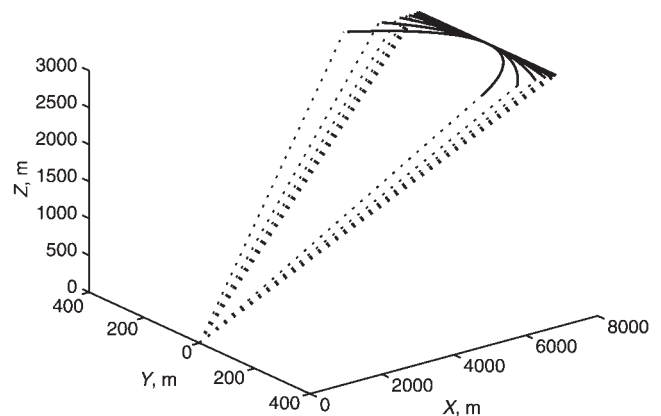

Fig. 4 *Receiver flight paths (shown as heavy lines) for α values of 0–0.0331*

The dotted lines show the receiver line-of-sight to scene centre at the aperture end points

Fig. 7 *Receiver flight paths (shown as heavy lines) for tilt angles from $-50°$ to $50°$*

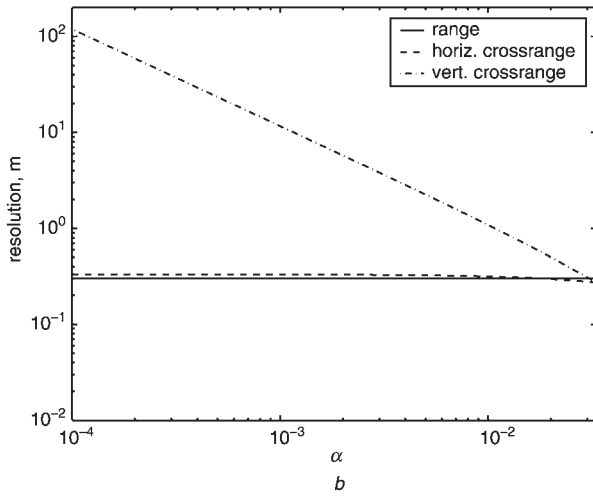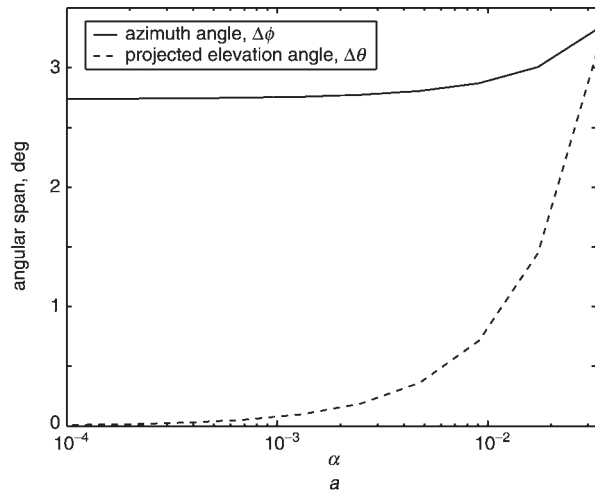The dotted lines show the receiver line-of-sight to scene centre at the aperture end points

Fig. 5 *Effects of receiver flight path eccentricity*

a Effect on angular spans of the data collection surface
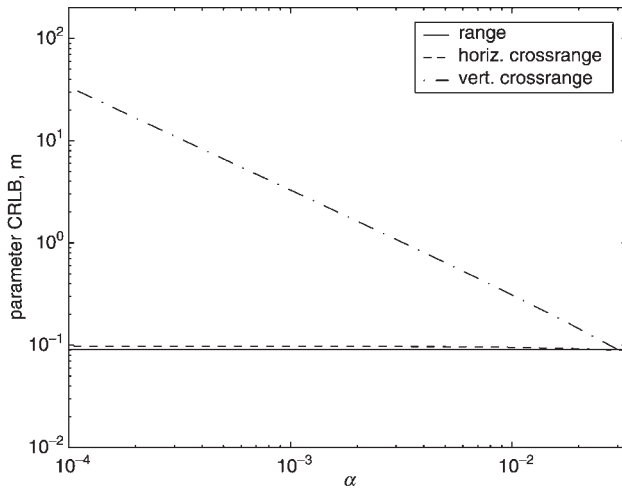*b* Effect on range, horizontal crossrange and vertical crossrange resolutions as computed from (18) and (21)

Fig. 8 *Effects of receiver flight path tilt*

a Effect on angular spans of the data collection surface
b Effect on range, horizontal crossrange and vertical crossrange resolutions
Angular spans are related to the crossrange resolutions via (18) and (21)

Fig. 6 *Effect of receiver flight path eccentricity on the performance of a parametric model scene reconstruction*

$\mathbf{F}^{-1}$, corresponding to the range, and horizontal and vertical crossrange, parameter estimate variances. Note the strong similarity between Figs. 5*b* and 6. This is not surprising, for filled apertures, the nonparametric resolution is known to be proportional to the parametric resolution, and they are expected also to be similar in the sparse aperture case. It is
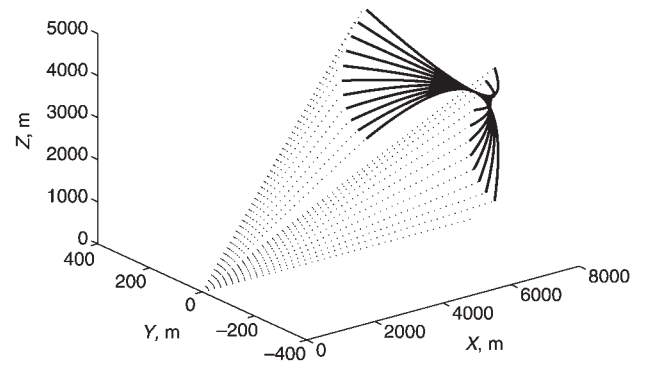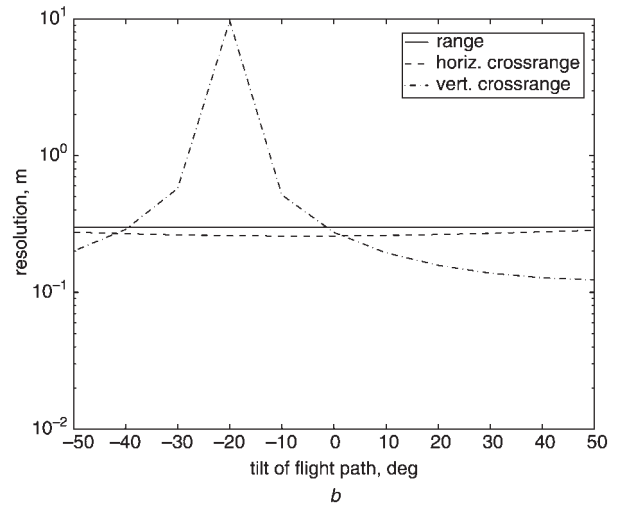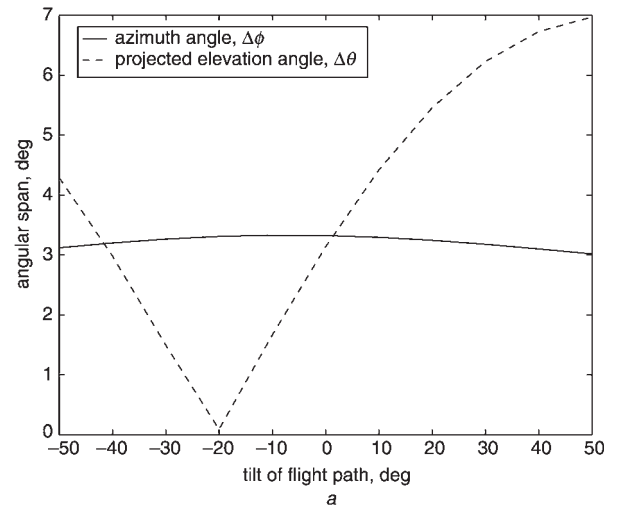
clear in both cases that added flight path eccentricity improves the reconstruction resolution. Note that the flight path length increases with increasing path eccentricity, which is why the vertical crossrange resolution improves without sacrificing horizontal crossrange resolution in this case.

In the second design example, we keep the eccentricity constant at $\alpha = 0.0331$ and we tilt the receiver flight path
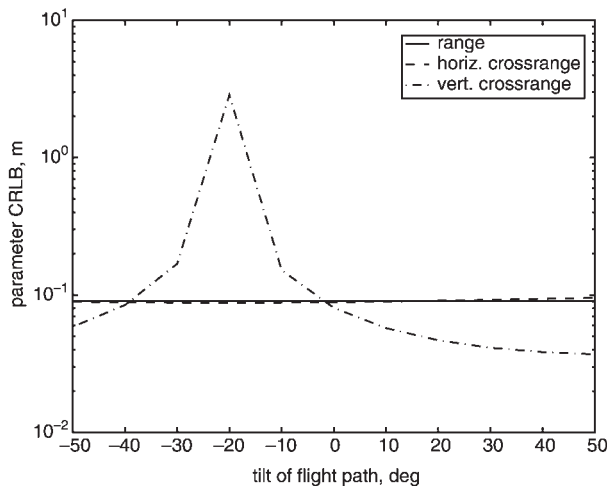
Fig. 9 *Effect of receiver flight path tilt on performance of a parametric model scene reconstruction*

Fig. 11 *Three-dimensional point scatterer, $r_0 = (0.23, 0.50, 0.67)$, reconstruction formed from phase history data collected by a receiver traversing a parabolic and tilted flight path*

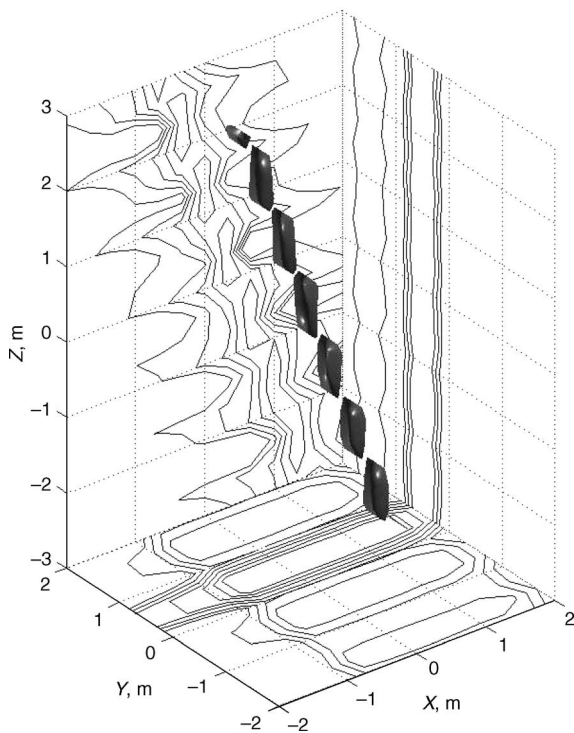−3 dB surface contour and projected contours in 5 dB increments

Fig. 10 *Three-dimensional point scatterer, $r_0 = (0.23, 0.50, 0.67)$, reconstruction formed from phase history data collected by a receiver traversing a linear flight path*

−3 dB surface contour and projected contours in 5 dB increments

about the line $Z = z_r(0)$, $X = x_r(0)$. By varying the amount of flight path tilt, as shown in Fig. 7 we achieve the angular spans plotted in Fig. 8*a*, the resolutions shown in Fig. 8*b* and the CRLB curves plotted in Fig. 9. One may therefore observe that, for the best 3-D resolution, the receiver flight path should not only be nonlinear, but the plane in which this path lies should be approximately orthogonal to the receiver line-of-sight. At a tilt angle of $-20°$, the receiver flight path is coplanar with the line-of-sight to scene centre; thus no out-of-plane resolution is possible.

To demonstrate the improvement realised by using both a curved and tilted receiver flight path, we generated two three-dimensional reconstructions of a point scatterer with position $r_0 = (0.23, 0.50, 0.67)$ using (5) and (11). Figure 10 shows a 3-D MF image reconstructed from data
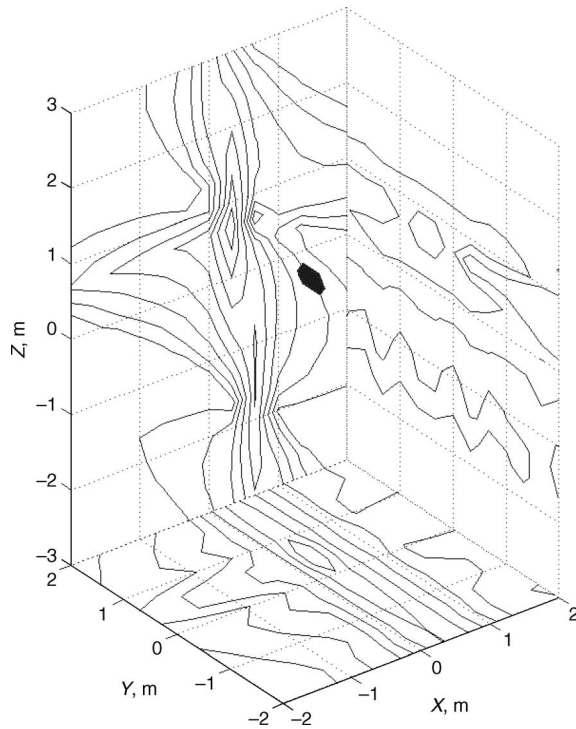
collected by a receiver flying the linear flight path of Fig. 4, and Fig. 11 shows a 3-D MF image reconstructed from data collected by a receiver flying the curved path with a tilt angle of $50°$ shown in Fig. 7. The ambiguities seen in Fig. 10 indicate a lack of resolution in the vertical crossrange direction; on the other hand, the 3-D localisation of the scattering centre is clearly seen in Fig. 11. The point scattering response in Fig. 11 is asymmetric due to the nonuniform frequency space sampling caused by the curved and tilted-receiver trajectory.

Li *et al.* [10, 11] and Knaell [12] present, for the monostatic case, an alternative method for exploiting the 3-D information encoded by nonlinear data collection geometries. If the data supporting Fig. 11 were used to form a 2-D image at $z = 0$ m (corresponding to the projection shown on the $x-y$ plane in Fig. 11), one would observe a point response smeared in crossrange by an uncompensated quadratic phase error, corresponding to the parabolic receiver flight path. The magnitude of this phase error is determined by the height of the scattering centre out of the ground plane. One may use autofocus algorithms [1, 2, 16] to estimate the magnitude of this phase error function, which then allows one to compute an estimate for the scatterer height. However, the presence of azimuth phase errors, due to uncompensated motion measurement errors, in the collected phase histories will confuse this method of height estimation, and overlapping lay-over of scatterers from different heights may also prevent 3-D localisation.

6 Conclusions

This paper has shown that the 3-D resolution of a bistatic SAR scene reconstruction is dependent on the dimensions of the data collection manifold. These dimensions may be manipulated through receiver flight path design to achieve finer resolution nonparametric 3-D reconstructions and

more accurate parametric estimates of 3-D information. We have demonstrated the validity of receiver flight path design through an example, and have shown that 3-D localisation of a point target was achieved in a 3-D MF reconstruction. Our analysis does not take into account practical consideration of motion measurement errors, or practical issues associated with executing nonlinear trajectories and motion compensation. However, the derived metrics give approximate lower bounds for 3-D resolution accuracy and give insight into the effects of flight trajectories on scene reconstruction performance. Both nonparametric and parametric resolution are effective tools for flight path design, thus allowing greatly improved 3-D resolution of the resulting reconstructed scene.

7 References

1 Carrara, W.G., Goodman, R.S., and Majewski, R.M.: 'Spotlight synthetic aperture radar: signal processing algorithms' (Artech House, Norwood, MA, USA, 1995)
2 Jakowatz, C.V., Wahl, D.E., and Eichel, P.H.: 'Spotlight-mode synthetic aperture radar: a signal processing approach' (Kluwer Academic Publishers, Boston, MA, USA, 1996)
3 Jakowatz, C.V., Jr., and Thompson, P.A.: 'A new look at spotlight mode synthetic aperture radar as tomography: imaging 3-D targets', *IEEE Trans. Image Process.*, 1995, **4**, (5), pp. 699–703
4 Graham, L.C.: 'Synthetic interferometer radar for topographic mapping', *Proc. IEEE*, 1974, **62**, pp. 763–768
5 Zebker, H., and Goldstein, R.: 'Topographic mapping from interferometric SAR observations', *J. Geophys. Res.*, 1986, **91**, pp. 4993–4999
6 Gabriel, A.K., and Goldstein, R.M.: 'Crossed orbit interferometry: theory and experimental results from SIR-B', *Int. J. Remote Sens.*, 1988, **9**, pp. 857–872
7 Desai, M.D.: 'Spotlight mode SAR stereo technique for height computation', *IEEE Trans. Image Process.*, 1997, **6**, pp. 1400–1411
8 Jakowatz C.V., Jr, Wahl, D.E., and Thompson, P.A.: 'Three-dimensional SAR imaging using cross-track coherent stereo collections'. Proc. 31st Asilomar Conf. on Signals, Systems and Computers, 1997, vol. 2, pp. 1199–1203
9 Rigling, B.D.: 'Physics, Fisher and phase: information content in SAR images'. Master's thesis, Ohio State University, OH, USA, 2000
10 Li, J., Bi, Z., Liu, Z.-S., and Knaell, K.: 'Using curvilinear SAR for three-dimensional target feature extraction', *IEE Proc., Radar Sonar Navig.*, 1997, **144**, pp. 275–283
11 Li, J., Wu, R., Stoica, P., Zelnio, E.G., and Bi, Z.: 'A robust hybrid spectral estimation algorithm for SAR imaging'. Conference Record of the 32nd Asilomar Conf. on Signals, Systems and Computers, November 1998, vol. 2, pp. 1322–1326
12 Knaell, K.: 'Three-dimensional SAR from curvilinear apertures'. Proc. IEEE National Radar Conf., May 1996, pp. 220–225
13 Soumekh, M.: 'Synthetic aperture radar signal processing with MATLAB algorithms' (Wiley–Interscience, Hoboken, NJ, USA, 1999)
14 Soumekh, M.: 'Reconnaissance with slant plane circular SAR', *IEEE Trans. Image Process.*, 1996, **5**, (8), pp. 1252–1265
15 Bryant, M.L., Gostin, L.L., and Soumekh, M.: '3-D E-CSAR imaging of a T-72 tank and synthesis of its SAR reconstructions', *IEEE Trans. Aerosp. Electron. Syst.*, 2003, **39**, (1), pp. 211–227
16 Rigling, B.D.: 'Signal processing strategies for bistatic synthetic aperture radar'. PhD thesis, Ohio State University, OH, USA, 2003, http://www.ohiolink.edu/etd/
17 Chiang, H., Moses, R.L., and Potter, L.C.: 'Model-based classification of radar images', *IEEE Trans. Inf. Theory*, 2000, **46**, (5), pp. 1842–1854
18 Potter, L.C., and Moses, R.L.: 'Attributed scattering centers for SAR ATR', *IEEE Trans. Image Process.*, 1997, **6**, (1), pp. 79–91
19 Gerry, M.J.: 'Two-dimensional inverse scattering based on the GTD model'. PhD thesis, Ohio State University, OH, USA, 1997
20 Potter, L.C., Chiang, D-M., Carriere, R., and Gerry, M.J.: 'A GTD-based parametric model for radar scattering', *IEEE Trans. Antennas Propag.*, 1995, **43**, (10), pp. 1058–1067
21 Van Trees, H.L.: 'Detection, estimation, and modulation theory, Part I' (Wiley, New York, NY, USA, 1968)

8 Appendix: Derivation of the Cramér–Rao lower bounds on the variance of 3-D scatterer position estimates

A well documented means for computing optimal achievable performance of unbiased estimators is the Cramér–Rao lower bound, as detailed in [21]. The CRLB for a parametric model gives the minimum variance that an unbiased estimator of that model can achieve in the presence of additive noise under a given distribution. The method for computing a CRLB is as follows. First, one must construct

Fisher's information (FI) matrix for the given parametric model and noise distribution. An FI matrix is a square with the number of rows equal to the number of parameters in the model. The elements of this matrix are defined as

$$F_{pq} = E\left\{ \left(\frac{\partial \log p(Y|\boldsymbol{\theta})}{\partial \theta_p}\right)^T \left(\frac{\partial \log p(Y|\boldsymbol{\theta})}{\partial \theta_q}\right) \right\} \quad (29)$$

where $E\{\cdot\}$ represents the expected value, θ_p is the pth model parameter and $\log(p(Y|\boldsymbol{\theta}))$ is the log-likelihood function of the observed random signal Y given the parameter vector $\boldsymbol{\theta}$. For example, if we were to construct a real-valued model of N samples with real additive white Gaussian noise, the likelihood function and log-likelihood functions would be

$$P(Y|\boldsymbol{\theta}) = \frac{1}{(2\pi\sigma^2)^{N/2}}\exp\left(\frac{-(Y - S(\boldsymbol{\theta}))^H(Y - S(\boldsymbol{\theta}))}{2\sigma^2}\right)$$
$$(30)$$

$$\log P(Y|\boldsymbol{\theta}) = -\frac{N}{2}\log(2\pi\sigma^2) - \frac{1}{2\sigma^2}(Y - S(\boldsymbol{\theta}))^H(Y - S(\boldsymbol{\theta}))$$
$$(31)$$

where σ^2 is the variance of the noise. Here, $S(\boldsymbol{\theta})$ is the estimated noiseless signal, defined by the parameter vector $\boldsymbol{\theta}$. Once the FI matrix has been constructed, the CRLB is found as the inverse of the FI matrix. The diagonal entries of the CRLB are the minimum achievable variances for any unbiased estimator of these parameters under the given noise conditions. By using the CRLB, one can predict the efficacy of a parametric model under noisy conditions, and in our case at a given resolution.

The CRLB for the model of (24) is obtained by computing and inverting the corresponding Fisher information matrix for a single point scattering centre with amplitude $A \exp(j\psi)$ and location (x, y, z). In this case, the parameter set $\boldsymbol{\theta}$ is $\{A, \psi, x, y, z\}$, and we will represent the mean complex signal of length N as a real-valued vector of length $2N$

$$\boldsymbol{s}(\boldsymbol{\theta}) = [s_{I,1}(\boldsymbol{\theta}), \ldots, s_{I,N}(\boldsymbol{\theta}), s_{Q,1}(\boldsymbol{\theta}), \ldots, s_{Q,N}(\boldsymbol{\theta})]^T \quad (32)$$

where $s_{I,i}(\boldsymbol{\theta})$ and $s_{Q,i}(\boldsymbol{\theta})$ represent the noiseless real and imaginary parts of the signal indexed by frequency sample. The likelihood function for this signal is

$$p(y|\boldsymbol{\theta}) = \frac{1}{(\pi\sigma^2)^N}\exp\left(-\frac{(y - \boldsymbol{s}(\boldsymbol{\theta}))^T(y - \boldsymbol{s}(\boldsymbol{\theta}))}{\sigma^2}\right) \quad (33)$$

and the log-likelihood function is

$$\log p(y|\boldsymbol{\theta}) = -N\log(\pi\sigma^2) - \frac{1}{\sigma^2}(y - \boldsymbol{s}(\boldsymbol{\theta}))^T(y - \boldsymbol{s}(\boldsymbol{\theta}))$$
$$(34)$$

where y is a noisy realisation of the signal with means $\boldsymbol{s}(\boldsymbol{\theta})$ and variance of $\sigma^2/2$ on each frequency sample.

Taking the derivatives of our log-likelihood function with respect to θ_p yields

$$\frac{\partial \log p(y|\boldsymbol{\theta})}{\partial \theta_p} = \frac{2}{\sigma^2}(y - \boldsymbol{s}(\boldsymbol{\theta}))^T\left(\frac{\partial \boldsymbol{s}(\boldsymbol{\theta})}{\partial \theta_p}\right) \quad (35)$$

which can be computed for each element of $\boldsymbol{\theta}$. Next, we compute each entry of the Fisher matrix

$$F_{pq} = E\left\{ \left(\frac{\partial \log p(y|\boldsymbol{\theta})}{\partial \theta_p}\right)^T \left(\frac{\partial \log p(y|\boldsymbol{\theta})}{\partial \theta_q}\right) \right\}$$

$$= \frac{4}{\sigma^4} \left(\frac{\partial \boldsymbol{s}(\boldsymbol{\theta})}{\partial \theta_p}\right)^T E\{(y - \boldsymbol{s}(\boldsymbol{\theta}))(y - \boldsymbol{s}(\boldsymbol{\theta}))^T\} \left(\frac{\partial \boldsymbol{s}(\boldsymbol{\theta})}{\partial \theta_q}\right)$$

$$= \frac{2}{\sigma^2} \left(\frac{\partial \boldsymbol{s}(\boldsymbol{\theta})}{\partial \theta_p}\right)^T \left(\frac{\partial \boldsymbol{s}(\boldsymbol{\theta})}{\partial \theta_q}\right) \tag{36}$$

which is equivalent to

$$F_{pq} = \frac{2}{\sigma^2} \left(\frac{\partial \hat{\boldsymbol{s}}(\boldsymbol{\theta})}{\partial \theta_p}\right)^H \left(\frac{\partial \hat{\boldsymbol{s}}(\boldsymbol{\theta})}{\partial \theta_q}\right) \tag{37}$$

where $\hat{\boldsymbol{s}}(\boldsymbol{\theta})$ is the complex valued vector $[s_{I,1}(\boldsymbol{\theta}) + js_{Q,1}(\boldsymbol{\theta}) \ldots s_{I,N}(\boldsymbol{\theta}) + js_{Q,N}(\boldsymbol{\theta})]^T$. The derivatives for the model of (24) are

$$\frac{\partial \hat{\boldsymbol{s}}(\boldsymbol{\theta})}{\partial A} = \exp[j\psi] \times \exp\left[j\frac{4\pi}{c}\left(xf_x(f,\tau) + yf_y(f,\tau) + zf_z(f,\tau)\right)\right] \tag{38}$$

$$\frac{\partial \hat{\boldsymbol{s}}(\boldsymbol{\theta})}{\partial \psi} = Aj\exp[j\psi] \times \exp\left[j\frac{4\pi}{c}\left(xf_x(f,\tau) + yf_y(f,\tau) + zf_z(f,\tau)\right)\right] \tag{39}$$

$$\frac{\partial \hat{\boldsymbol{s}}(\boldsymbol{\theta})}{\partial x} = Aj\frac{4\pi f_x(f,\tau)}{c}\exp[j\psi]$$
$$\times \exp\left[j\frac{4\pi}{c}\left(xf_x(f,\tau) + yf_y(f,\tau) + zf_z(f,\tau)\right)\right] \tag{40}$$

$$\frac{\partial \hat{\boldsymbol{s}}(\boldsymbol{\theta})}{\partial y} = Aj\frac{4\pi f_y(f,\tau)}{c}\exp[j\psi]$$
$$\times \exp\left[j\frac{4\pi}{c}\left(xf_x(f,\tau) + yf_y(f,\tau) + zf_z(f,\tau)\right)\right] \tag{41}$$

$$\frac{\partial \hat{\boldsymbol{s}}(\boldsymbol{\theta})}{\partial z} = Aj\frac{4\pi f_z(f,\tau)}{c}\exp[j\psi]$$
$$\times \exp\left[j\frac{4\pi}{c}\left(xf_x(f,\tau) + yf_y(f,\tau) + zf_z(f,\tau)\right)\right] \tag{42}$$

which are complex-valued vectors indexed by frequency and slow time samples. Finally, the CRLB of our parameter set is defined to be inverse of the Fisher matrix, $\boldsymbol{F}^{-1}$; the lower bound on the variance of each parameter is given by the corresponding diagonal element of $\boldsymbol{F}^{-1}$.